Polymer 281 (2023) 126114

Contents lists available at ScienceDirect

Polymer

journal homepage: www.elsevier.com/locate/polymer

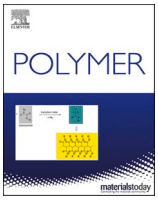

Simulation study of shape memory polymer networks formed by free radical polymerization

Collin D. Wick [a,*], Andrew J. Peters [a], Guoqiang Li [b]

[a] College of Engineering & Science, Louisiana Tech University, Ruston, LA, 71270, USA
[b] Mechanical & Industrial Engineering Dept, Louisiana State University, Baton Rouge, LA, 70803, USA

A B S T R A C T

Chemically crosslinked thermoset shape memory polymers (TSMPs) can combine the strength required for load-carrying structures and devices with stimuli-responsive properties that can allow them to perform crack-closing or other multifunctional properties. In particular, UV-curable shape memory polymers can be used for 3D printing, and to enhance the design process, a molecular dynamics (MD) modeling framework was developed to study them. The MD simulations were used to calculate thermophysical, mechanical, and shape memory properties for glycerolate dimethacrylate after UV-curing to form a polymer network. Semi-quantitative agreement between simulation and experiment was achieved for the different properties compared. By examining various conditions for network formation, a range of distinct cross-linking topologies were generated and their effects on properties were evaluated. In particular, it was found that the percentage of monomers with the maximum number of possible links with other monomers had a greater correlation with recovery stress than the number of monomers reacted overall. A new topological fingerprint, the average minimum pathway between monomers, was proposed and found to have the strongest correlation with recovery stress than all properties examined.

1. Introduction

Chemically crosslinked thermoset polymers have been widely used in load-carrying structures and devices due to their exceptional mechanical properties, thermal stability, chemical resistance, and ease of manufacturing [1]. In recent years, researchers have designed, synthesized, and tested multifunctional thermoset polymers with various capabilities including a shape memory effect (SME) [2], the ability to self-heal and recycle [3], flame retardancy [4], 3D printability [5], and combinations of two or more functionalities in one material [6]. Among these polymers, those that exhibit SME are particularly noteworthy, because they enable broader applications beyond simple load carrying. For instance, they can serve as a crack-closing device using the close-then-heal strategy in damage healing [7], as deployable structures [8], as sealant in pavement and bridge deck joints [9], and as proppant or loss circulation materials in geothermal [10] and oil & gas drilling [11].

The fundamental requirement for a polymer to posses the SME is a stable network and a switching phase [12]. The stable network can be molecular entanglement, chemical crosslinks, crystallization, or an interpenetrating network [13], while the switching phase can be a crystallization/melting transition, a vitrification/glass transition, an anisotropic/isotropic transition, reversible crosslinking, or supramolecular association/dissociation [13,14]. The presence of a crosslinked network in thermoset polymers has resulted in many of these materials exhibiting the (SME), while the switching phase is usually associated with the glass transition temperature.

4D printing has gained significant attention as a research topic in the additive manufacturing of polymer composite materials [15]. In 4D printing, shape memory polymers are often used as ink [16]. Free-radical polymerization has been widely employed for 4D printing SMPs using several types of printers such as digital light processing (DLP) printers [17] and direct ink writing (DIW) printers [18]. The quality of 4D-printed SMP parts is determined by the light intensity (typically ultraviolet (UV) light), exposure time, printing speed, printing layer thickness, and curing kinetics [19]. Therefore, understanding the free-radical polymerization of TSMPs is critical to manufacturing high-quality 4D-printed TSMP parts. While some studies have been conducted to understand the curing kinetics of photopolymerization of TSMPs [21], the emphasis has been on elucidating the effect of various process parameters on the degree of curing. More studies are needed to explain the curing process at the molecular length scale.

Molecular dynamics (MD) simulations have a long history in the modeling of polymers, calculating their mechanical and shape memory properties to elucidate structure-property relationships [20–25]. These also include the MD study of polymers that are cured by free-radical

* Corresponding author.
E-mail address: cwick@latech.edu (C.D. Wick).

https://doi.org/10.1016/j.polymer.2023.126114
Received 2 May 2023; Received in revised form 6 June 2023; Accepted 12 June 2023
Available online 13 June 2023

polymerization [26]. We previously studied the shape memory properties of amine-hardened epoxies, but to our knowledge, the study of shape memory properties of TSMPs cured by free-radical polymerization has not been performed by MD, and this study fills that gap. We develop a framework for studying the curing process and validate our approach against experimental data. The details of the networks formed for different initiator concentrations and ultimate crosslinking percentage are then investigated and discussed.

2. Simulation details

2.1. Initial equilibration

The polymer network was formed out of the monomer bisphenol A glycerolate dimethacrylate (BPAGMA) (see Fig. 1). Polymer networks formed from this monomer have been extensively studied with experimental measurements for thermophysical, mechanical, and shape memory properties [27]. The ligpargen software [28] was used to create the initial structures for BPAGMA, in which the monomer has 73 atoms. The software uses SMILES [29] for the monomers as input and creates files containing the structure of the monomer and the OPLS forcefield parameters [30–32]. All calculations, unless stated otherwise, used a potential truncation of 9 Å with the particle mesh Ewald summation technique to account for long-ranged interactions [33].

After the creation of a single monomer in a small cubic box, the system was replicated 7 × 7 × 7 to create a large cubic box with dimensions of around 150 Å on each side. The total system size after replication included 343 monomers and 25,039 atoms. This size is similar to what was found to give consistent shape memory properties for polymer networks in our previous work [34,35]. The LAMMPS simulations software package [36–38] was used to carry out the equilibration in the NpT ensemble with the Nose Hoover thermostat and barostat [39,40] at a temperature of 398 K. Hydrogen atomic positions were kept rigid with the SHAKE and RATTLE algorithms [41]. To compress the system, a 75 ps simulation run was carried out at 10 atm at a timestep of 0.25 fs to shrink the system to a liquid. Another 125 ps of equilibration at 1 atm was carried out after this initial compression. Next, the timestep was increased to 0.5 fs, and 500 ps equilibration at 1 atm was carried out. After this, an additional 500 ps of simulations were carried out, saving the configuration every 100 ps to create five independent systems configurations.

2.2. Creation of networks

The five independent systems were cross-linked using a free radical polymerization process similar to previously used methods [26]. We employed this method because of its success in generating diverse polymer systems based on the free radical chain reaction mechanism. Previous BPAGMA experiments used an initiator concentration of 3 wt% [27]— equivalent to 9 mol%. For the simulations, the initiator molecules weren't explicitly modeled, but a certain number of alkenes were randomly activated as shown in Fig. 2 (a). The actual "I" used in this work was an H atom, creating a methyl group adjacent to a tertiary alkene carbon (see Fig. 2(b)). Fig. 1 shows that there are two alkene groups per BPAGMA monomer, residing on their ends, which will be denoted as end alkene groups (EAG). So, the upper bound of the number of potential reactive groups that can be initiated are 4.5% of all EAGs. The system had 343 total monomers, resulting in 686 EAGs, all of which were potential reactive groups. Three different concentrations of initiated EAGs were considered: 7/686 (~1%), 21/686 (~3%), and 31/686 (~4.5%).

After the initiation of the system, propagation and termination of the reactions were carried out in cycles, as summarized in Fig. 3. For each cycle, a three-step procedure was used. **1)** An MD equilibration of 10,000 steps (5 ps) in the NVT ensemble, followed by 10,000 steps (5 ps) in the NpT ensemble was carried out at a temperature of 398 K and 1 atm. The reason for doing the initial NVT simulation was to assure the system was stable before allowing the volume to fluctuate. **2)** The distance between all reactive tertiary EAG carbons, shown with a dot in Fig. 2, and non-reacted primary EAG carbons were calculated (see Fig. 2 (b)). Also, the distance between all reactive EAG carbons themselves was calculated (see Fig. 2(d)). The shortest distance of these within a 5 Å cutoff was chosen to react. If the shortest distance was between two reactive EAG carbons, a termination by combination reaction occurred (see Fig. 2(d)); otherwise, a propagation reaction occurred (see Fig. 2 (c)). If no distances within the cutoff were found, then the next cycle was run with no new reaction. **3)** As with previous work [34], the reaction was performed by creating a bond between the reacting atoms with the equilibrium length prescribed by the OPLS force field [30–32], but with a weak 5 kcal/mol/Å^2 force constant. All other topological interactions (van der Waals, angular, and dihedral) were taken to match what is generated from a polymer fragment given with the ligpargen software [28] for the OPLS force field [30–32]. A conjugant gradient energy minimization followed this to gradually bring the reacting atoms together, followed by increasing the force constant to the OPLS force field value and minimizing the structure again. Both propagation and termination reactions were handled in this manner, but termination reactions were relatively rare, occurring once every few hundred reaction cycles.

A total of 500 cycles were carried out for each independent system, saving the system configurations every 50 cycles. Since not all of the potential cycles result in reactions, each of the five independent systems had somewhat different numbers of successful reactions. Experimentally, the final ratio of monomers that were part of a network was between 75 and 80% for BPAGMA [27]. For each of the independent systems, the saved cycle with over 78% of the monomers reacted (i.e., with at least one of its two alkene groups reacted) was chosen, which required approximately 400 cycles for each. The actual number of monomers reacted ranged from 78 to 82%, which required 53–59% of EAGs to be reacted.

2.3. Calculation of thermal and mechanical properties

The glass transition temperature (T_g) was calculated using a procedure identical to that described in previous work [34]. The specific details for calculating T_g are given in section S1 of the supporting

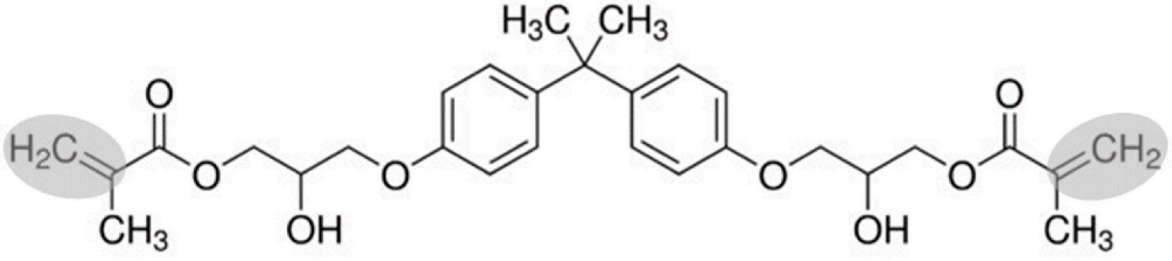

Fig. 1. Structure for bisphenol A glycerolate dimethacrylate (BPAGMA) with the end alkene groups (EAGs) shaded.

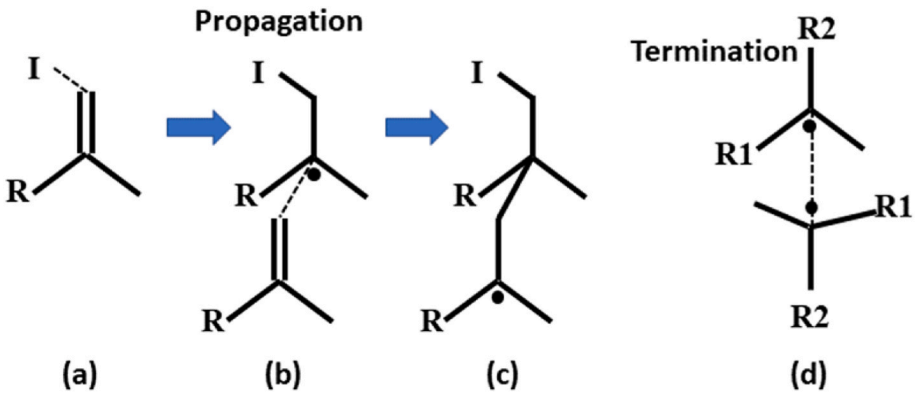

Fig. 2. Schematic of the free radical chain reaction mechanism used in this work.

information. The Young's modulus was calculated for both the rubbery states (at 30 K higher than T_g) and glassy states (at 298 K) following the procedure used in previous work [34]. The specific details used for calculating the Young's moduli are given in section S2 in the supporting information.

2.4. Calculation of shape memory properties

To calculate recovery stress, a multistep process somewhat similar to our previous work [34] was carried out as outlined in Fig. 4. The first step is **1)** programming, which was carried out by compressing the system at a continuous rate by 40% in one direction over a period of 4 ns with the pressure perpendicular to the deformation set to 1 atm. For each of the five independent systems, all three dimensions were programmed separately to create a total of 15 programming simulations. The procedure usually resulted in a very large programming stress, much higher than with the step-growth polymerization reactions carried out previously [34]. **2)** To help alleviate this to a degree, additional annealing simulations were carried out after programming. These included 1 ns of heating to 600 K at constant volume, and an additional 1 ns of constant volume annealing at 600 K. After that, a 1 ns cooling step to 30 K above T_g was run at fixed strain in one dimension but pressure set to 1 atm in the other two dimensions. This step was followed by 1 ns of further equilibration at fixed temperature and linear strain to create relaxed systems. The average stress during the last 50 ps of this run was the relaxation stress, σ_{relax}.

The programmed, annealed and relaxed systems were then **3)** cooled to 298 K (glassy state) over a 4 ns period at a fixed linear strain, (still retaining 40% compression of the original shape) (ε_i), and then allowed to fully relax for 4 ns at 298 K at 1 atm. During this relaxation, fluctuations in volume were allowed to occur, and an elastic rebound or "spring-back" occurs, causing a small change in strain to a new value (ε_f) [42]. The change in strain during this step was used to define the shape fixity ratio (F),

$$F = \frac{\varepsilon_f}{\varepsilon_i} \times 100\% \quad (1)$$

Next, the systems were **4)** warmed at fixed strain in the direction of programming, still allowing lateral directions to relax, for 4 ns to 30 K higher than T_g, followed by an additional 4 ns of equilibration at fixed strain at 30 K higher than T_g. The average stress during the last 0.5 ns of this last step in the rubbery state was used to determine the recovery stress, σ_{rec}.

3. Results and discussion

3.1. Thermodynamic and mechanical properties

The T_g, glassy Young's modulus (E_{glassy}), and rubbery Young's modulus ($E_{rubbery}$) for different initiator rates (1, 3, and 4.5%) and reaction % were calculated and are given in Table 1. As stated above, the initiator rate is defined as the percentage of monomers that have one of their two EAGs initiated. The reaction % is the percentage of monomers that participate in a reaction. If any of the two EAGs in a monomer form a bond with another monomer, it is considered reacted. It can be observed that increasing the initiator concentration has little impact on T_g, except that the uncertainty, calculated from the standard error of the mean, is higher for lower initiator concentrations. Two T_g values were identified experimentally, 75 and 158 °C (348 and 431 K) [27]. The fact that there were two was stated to be the result of different cross-linking densities throughout the samples. The value calculated from the simulations is in between those two, closer to the higher one, which is expected as T_g is generally overestimated for polymers using molecular simulation [43].

The experimental values for Young's modulus are estimated from experimental stress-strain curves at different temperatures (Fig. S4 in the supporting information in Ref. [27]). E_{glassy} is somewhat underpredicted with respect to experiment, but reasonably close and of similar agreement with what was found for many thermoset polymers [44]. Higher initiator concentration slightly reduces this value, though the difference is not significant. $E_{rubbery}$ is also underpredicted in comparison with experiment, and decreases when the initiator concentration is higher than 1%, though it did not change with further increases. Again, this is of similar agreement with what was found for other thermoset polymers [44]. The ratio of E_{glassy} to $E_{rubbery}$ can sometimes be related to its shape memory properties [12], and is also shown in Table 1. For those TSMPs using entropy reduction as the primary energy storage mechanism, the larger the ratio between E_{glassy} to $E_{rubbery}$, the higher the shape recovery ratio should be. Recently, TSMPs with energy storage through enthalpy increase by bond length and angle change have been synthesized [45]. For these TSMPs, due to the contribution to energy storage by both entropy reduction and enthalpy increase, even with lower E_{glassy} to $E_{rubbery}$ ratios, the TSMPs can still exhibit excellent shape memory effect, in addition to the much higher stress memory [21,38].

From Table 1, the experimental value is similar to the simulation values with 1% initiator concentration, but nearly twice as high for the other two initiator concentrations at 80% reaction. Reducing the reaction to 70% results in a small decrease in E_{glassy}, but has a profound effect on $E_{rubbery}$, which decreases by a similar amount as for the 80% reaction systems. This is consistent with what was found for epoxy-hardener based TSPMs [46]. This results in a ratio of E_{glassy} to $E_{rubbery}$ increasing by a factor of 2.5.

3.2. Shape memory properties

The stress after programming, annealing, and relaxation (σ_{relax}), the shape fixity ratio (F), and the recovery stress (σ_{rec}) were calculated and are given in Table 2 for the same initiator concentrations and

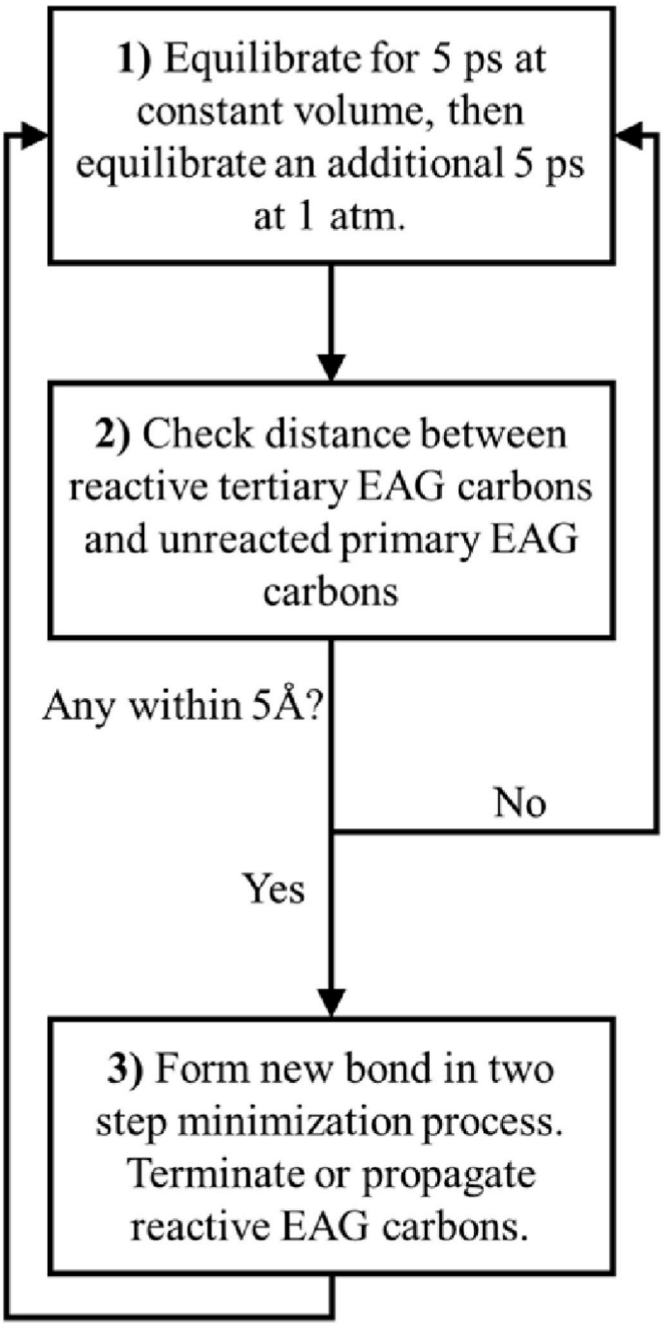

Fig. 3. Flowchart for free radical chain reaction cycle.

crosslinking percentages shown in Table 1. As stated in section II.C, the relaxation stress, σ_{relax}, is the stress after 40% compression programming, followed by annealing at elevated temperature, and cooling at fixed strain to 30 K higher than T_g. The relaxation stress decreases significantly with increasing initiator concentration. A similar trend is observed for σ_{rec} as for σ_{relax}, significantly decreasing with increasing initiator concentration. However, the ratio of recovery stress to relaxation stress, $\sigma_{rec}/\sigma_{relax}$, increases with initiator concentration. This shows that higher initiator concentration may cause the system to retain a higher fraction of the stress through the cooling and recovery cycles. This is also consistent with the results of the shape fixity ratio (Table 2). The shape fixity ratio is related to the elastic spring-back (see section II. C) that occurs when the network is relaxed in the glassy state, with a lower fixity coinciding with a larger spring-back. The lower initiator concentrations have more elastic spring-back. It would follow that greater elastic spring-back should relieve more stress in the system, decreasing the amount of recovery stress compared to the stress after relaxation.

A question may arise if the lower $\sigma_{rec}/\sigma_{relax}$ and F for systems with lower initiator concentration were more a consequence of the network topology or the fact that they were programmed to a higher stress (a consequence of programming to the same strain). To study this further, the system with 1% initiator concentration was programmed to have a similar relaxation stress as the system with the 4.5% concentration, which required compressing the system less than the others, by 30% of its original size. All values, the shape fixity ratio, the relaxation stress, and the recovery stress, were nearly identical to those with the 4.5% initiator concentration. This suggests that the 1% initiator case creates a stiffer material, but similar amounts of stress are stored during programming.

At the highest initiator concentration, two percentages (70% and 80%) of monomers reacted were examined, one lower than experiment [27], and the other at the higher end of the experimental range. With a higher percentage of monomers reacted, the relaxation and recovery stresses increase significantly as is expected. However, the increase in recovery stress is much larger than the increase in relaxation stress, leading to a much higher $\sigma_{rec}/\sigma_{relax}$ ratio for the system with 80% of the monomers cross-linked. This shows that maximizing the number of monomers that react is an important factor in increasing the amount of recovery stress gained from the same programming stress. In summary, two factors contribute to higher recovery stress: lower initiator concentration (because the material is stiffer and therefore the programming stress is higher for the same strain) and higher reaction %. Higher reaction %, in particular, is important for retaining a high amount of recovery stress with respect to the amount of relaxation stress applied to the sample.

For all systems, the relaxation stress is much higher than experiment. This is expected due to the short simulation times, which are many orders of magnitude shorter than that for experimental measurements. For the same reason, the recovery stress is expected to be significantly overpredicted as well. However, both should be semi-quantitatively consistent between different systems. It was found that computational predictions for recovery stress were approximately three times higher than experiment for relaxation and recovery stress in previous work examining epoxy-based TSMPs [34,47]. The system with an initiator concentration of 4.5% and 70% of the monomers crosslinked has a recovery stress twice as high as experiment, while the system with an initiator concentration of 4.5% and 80% of the monomers crosslinked is 3.8 times higher than experiment. Since the experimental system had a monomer reaction rate between 75 and 80% [27], the values calculated appear to be consistent with an approximately threefold overprediction compared to experiment, as found previously [34]. In summary, the relaxation and recovery stresses are overpredicted in comparison with experiment, but consistent with our previous work when conditions, such as initiator concentration and reaction % are the same as experiment [34,47].

3.3. Monomer binding environment

The only difference between the individual networks investigated is the topology. To study this in greater detail, the number of distinct monomers bound to a given EAG was calculated. There can be up to two possible reactions that an EAG can have, as shown in Fig. 2. The average percentages of EAGs bonded with zero, one, and two monomers, from the five independent simulations, are given in Table 3. The number of unbonded EAGs are similar between the systems with the same reaction %. The biggest difference between them is in the ratio of one-bonded to two-bonded EAGs. The higher initiator concentration results in more one-bonded EAGs at the expense of fewer two-bonded EAGs. In fact, if termination by combination is rare and the initiated sites do not frequently react again, this must be the result. In that case, each initiator

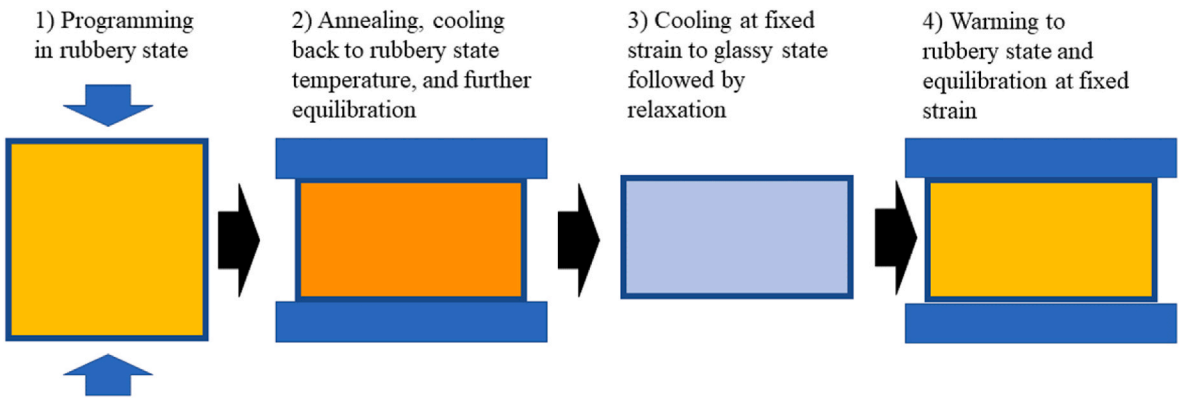

Fig. 4. Schematic of the 1) programming, 2) annealing, 3) cooling, and 4) warming process used to calculate shape recovery.

Table 1
Glass transition temperature (T_g), and Young's modulus in the glassy and rubbery states for different initiator concentrations and percentages of reacted monomers (in parenthesis) for BPAGMA, compared with experiment [27].

	Initiator % and (reaction %)	T_g(K)	E_{glassy} (GPa)	$E_{rubbery}$ (GPa)	$E_{glassy}/E_{rubbery}$
Sim	1% (80%)	393 ± 11	1.33 ± 0.09	0.10 ± 0.01	13
	3% (80%)	408 ± 10	1.24 ± 0.06	0.054 ± 0.004	23
	4.5% (80%)	399 ± 4	1.21 ± 0.06	0.063 ± 0.004	19
	4.5% (70%)	403 ± 9	1.02 ± 0.08	0.021 ± 0.004	49
Exp	4.5% (75–80%)	348–431	~2.1	~0.19	11

Table 2
Stress after relaxation (σ_{relax}), recovery stress (σ_{rec}), their ratio, and shape fixity ratio (F) for different initiator concentrations and percentages of reacted monomers (in parenthesis) for BPAGMA, compared with experiment [27].

	System	σ_{relax}(MPa)	σ_{rec}(MPa)	$\sigma_{rec}/\sigma_{relax}$	F
Sim	1% (80%)	120 ± 6	81 ± 4	0.68	96.4
	1% (80%)[a]	63 ± 5	51 ± 3	0.81	98.3
	3% (80%)	89 ± 6	67 ± 4	0.75	98.1
	4.5% (80%)	62 ± 5	51 ± 3	0.82	98.6
	4.5% (70%)	50 ± 3	27 ± 3	0.54	100
Exp	4.5% (75–80%)	28	13.4	0.48	93–100

[a] System compressed by 30% of its original size (vs. 40% for the rest).

will have a one-bonded EAG where it initiated, and a one-bonded EAG where it stopped growing. The two-bonded and unbonded EAGs are then necessarily determined by the % reaction. Comparing the results in Table 3 with Tables 1 and 2, It is clear that more two-bonded EAGs is correlated with greater stiffness and recovery stress.

After considering the EAG local bonding environment, the bonding environment of the monomer as a whole can be considered. Since each monomer has two EAGs, they can bind to up to four other monomers. Table 4 gives the average number of monomers (averaged over five independent simulations) bonded to zero, one, two, three, and four other monomers, along with the percentage of monomers in the largest network, and the average number of bonds formed with other monomers. For all of the systems studied, the largest network is very similar to the overall reaction %, indicating that nearly all of the monomers that participate in a reaction are a part of one network. Principally, the systems have a single large network with the remaining monomers being unreacted. The number of bonds per monomer shows that with a higher initiator concentration, there are fewer monomers with both two and four bonds. This is consistent with the average number of bonds per

Table 3
Percentage of EAGs bonded with zero, one, and two other monomers.

System	Unbonded EAGs	One-bonded EAGs	Two-bonded EAGs
1% (80%)	45%	2%	53%
3% (80%)	43%	6%	51%
4.5% (80%)	43%	9%	48%
4.5% (70%)	53%	9%	38%

EAG, which are primarily compromised of zero or two bonds. With a higher number of bonds per monomer, it would be expected that the total number of bonds in the network would also increase. One would expect having more bonds per monomer would create more bonds within a network overall, which would make the network stiffer, and is consistent with the moduli results given in Table 1. Also, it would be expected that more bonds within a network would increase the relaxation and recovery stress, consistent with the results shown in Table 2.

To better quantify the influence of the topological properties described in the previous paragraph, their Pearson correlation coefficient (CC) with the recovery stress were calculated and the results are given in Table 4. The two highest correlating properties are the percentage of monomers with one bond and with four bonds. Monomers with only one bond, while connected to the network, will always represent end-segments, which will not contribute to percolating the network. This is why they are negatively correlated with recovery stress to a significant degree. The number of bonds per reacted monomer is also strongly correlated with recovery stress, but less so than the number of 4-bonded monomers, indicating that the slightly higher number of bonds per monomer for lower initiator content is not the most important factor at play; the number of 4-bonded monomers (which are the main source of crosslinking) are more important, and more of those are created when using a lower initiator concentration.

Comparing the systems with 70 and 80 reaction %, the largest difference is the number of monomers with zero bonds. However, nearly as significant is the fact that the 70% and 80% systems have nearly the same number of 2-bonded monomers, but very different numbers of 4-bonded monomers. That is, between these two systems, nearly all the 4-bonded monomers that were lost resulted in unbonded monomers. It is these 4-bonded monomers that best extend the network, so the network quality is significantly reduced. 2-bonded monomers aren't terminal points, so they don't hurt the network, but neither do they extend it. In previous work on investigating topology for thermoset shape memory polymers, it was suggested that a "perfect" network was one in which all monomers had a maximum number of bonds with others [48]. It was shown that having closer to this perfect network was correlated with an increase in recovery stress, which is consistent with all the results presented.

Table 4
Percentage of monomers bonded to zero up to four other monomers, along with the percentage of monomers in the largest network and the average number of bonds with other monomers per reacted monomer. The correlation coefficient (CC) between each of these with the recovery stress (σ_{rec}).

System	Number of bonds per monomer					Percentage of monomers in the largest network	Number of bonds per reacted monomer
	0	1	2	3	4		
1% (80%)	21%	2%	47%	2%	28%	79%	2.71
3% (80%)	19%	5%	42%	8%	26%	81%	2.68
4.5% (80%)	20%	8%	40%	10%	23%	80%	2.63
4.5% (70%)	30%	9%	39%	7%	15%	71%	2.38
CC with σ_{rec}	−0.80	−0.95	0.90	−0.54	0.98	0.79	0.94

3.4. Overall network topology

To better gauge overall topology, the average minimum path length in terms of the number of links between monomers ($<N_{links}>$) was calculated for each system. This property should be related to how compactly a network is bound, as a larger value indicates a more extended and more imperfect network. Breaking an existing bond without breaking the entire network will result in some of the minimum paths being longer (those that would have gone through the broken bond) but no shorter minimum paths. Based on previous results [48], we conjecture that more compact networks would, in general, have greater stiffness and higher recovery stress. A more compact network (indicated by a smaller average minimum path length) means that any stress caused by a deformation would be distributed across more links, thus stiffening and strengthening the system. In addition to the systems studied, a periodic diamond network (based on a diamond cubic crystal structure where the nearest neighbors are bonded) was created as a comparison for this analysis, in which each monomer in the network was bound to exactly four other monomers in a tetrahedral pattern (see Fig. 5), thus creating a perfect network. The diamond network size was set to match the size of the largest network for the different systems. Since there were 343 monomers total in each system, the average size of the largest network in the 70% and 80% reacted systems were approximately 240 and 274 monomers, respectively. The diamond network should be relatively cubic, and each diamond unit cell has a total of 8 sites.

To get a number of sites close to the number of monomers for the systems studied, a lattice size of the diamond network of $3 \times 3 \times 4$ can be used, totaling 288 monomers. To improve linkage between a diamond network and the two systems studied, different diamond networks were created, ranging from $2 \times 2 \times 2$ to $4 \times 4 \times 4$ having all possible combinations in between with the constraint that any one lattice number is no more or less different than another by one (i.e., $2 \times 2 \times 4$ is not considered). The results are shown in Fig. 5, and a cubic fit between the average number of links with respect to the number of sites. It can be observed that the fit is quite good, which gives the following relationship,

$$< N_{links} >= 3.1724 + 0.018629 N_{sites} - 3.2863 \times 10^{-5} N_{sites}^2 + 2.4977 \times 10^{-8} N_{sites}^3 \quad (2)$$

Table 5 gives the average minimum number of links between monomers for the different systems studied, compared with the same property for the diamond network as described previously based on the average number of monomers in the largest network. Increasing the initiator concentration results in an increase in the average number of links between monomers. Furthermore, the system with the lower reaction %, while having a smaller sized network overall, has a higher number of links in-between monomers, signifying a more extended network. This is related to the fewer number of monomers with four bonds as described in the previous section. To quantify the role of the average number of links between monomers as a fingerprint for polymer networks, the CC of the ratio of $< N_{links}^{sim} > / < N_{links}^{DN} >$, as shown in Table 5, with the recovery stress is −0.9956, being more significant than any of the properties related to the monomer binding environment. As this is a global descriptor, it makes sense that it outperforms local descriptors.

Table 5
Average number of links along the minimum path between monomers ($< N_{links} >$) for the different systems studied (sim), along with for the diamond network (DN) with the same number of monomers as in the largest network. The ratio of the two values is also given.

System	$< N_{links}^{sim} >$	$< N_{links}^{DN} >$	$< N_{links}^{sim} > / < N_{links}^{DN} >$
1% (80%)	6.5	6.32	1.03
3% (80%)	7.4	6.32	1.17
4.5% (80%)	8.0	6.32	1.27
4.5% (70%)	9.2	6.10	1.58

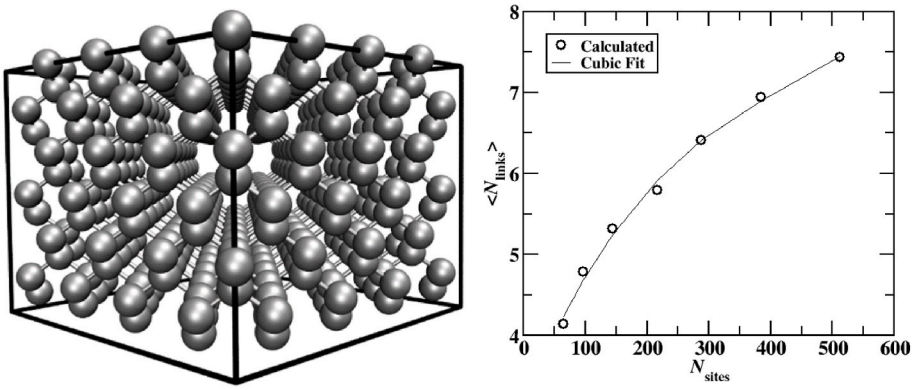

Fig. 5. Visualization of the diamond network (left). Bonds that wrap around the periodic boundary are not shown. Each bead represents a monomer. Average minimum number of links between sites as a function of the number of diamond lattice sites (right), along with a cubic fit of the data.

4. Conclusions

A molecular dynamics (MD) modeling framework was developed to model free-radical polymerized and UV-curable shape memory polymers. The results from the MD simulations were used to calculate thermophysical properties, mechanical properties, and recovery stress of bisphenol A glycerolate dimethacrylate and compared with experimental results. Reasonably good agreement was achieved with experiment for the glass transition temperature, along with glassy and rubbery moduli. Semiquantitative agreement with experiment for recovery stress, consistent with previous work, was achieved. Two network creation conditions were investigated: the initiator concentration rate, and the percentage of monomers that are reacted. A higher initiator concentration caused a moderately lower network stiffness in both the glassy and rubbery states, and a moderately lower recovery stress. With a higher proportion of monomers that were reacted in a polymer network, the glassy Young's modulus increased a moderate degree, while the rubbery modulus increased a large amount. The recovery stress was also increased with a higher percentage of monomers being reacted.

An analysis of network topology found that the number of monomers with one bond had a strong negative correlation with recovery stress. Higher initiator concentration results in more single-bonded monomers, so decreasing this could lead to networks with higher recovery stress. Additionally, a higher number of monomers with four bonds, the maximum number of bonds allowable, was strongly correlated with higher recovery stress. A lower initiator concentration and a higher proportion of monomers reacted led to a higher proportion of monomers with four bonds. The results also show that while more unbonded monomers, which is what is used to determine the reaction %, is negatively correlated with recovery stress, having fewer fully bonded monomers has the larger impact. Further investigation identified another topological fingerprint, the average number of links along the minimum path between monomers, to be a reasonable measure of how 'compact' a network is, with fewer links representing a more compact network. This topological fingerprint had the highest correlation with recovery stress than all other parameters investigated.

The results of this work have provided a pathway for using MD to semi-quantitatively predict the recovery stress, along with identifying and calculating topological fingerprints. These will be used to study new polymers and create a dataset for machine learning that will be used to guide experimentalists in which systems hold the most promise for improved recovery stress. Finally, the results of this work show that for creating networks with the highest possible recovery stress, the lowest initiator rate that maintains a high reaction rate should be sought.

CRediT authorship contribution statement

Collin D. Wick: Conceptualization, Methodology, Writing – original draft. **Andrew J. Peters:** Conceptualization, Writing – review & editing. **Guoqiang Li:** Conceptualization, Project administration.

Declaration of competing interest

The authors declare that they have no known competing financial interests or personal relationships that could have appeared to influence the work reported in this paper.

Data availability

Data will be made available on request.

Acknowledgements

This work is supported by the US National Science Foundation under grant number OIA-1946231 and the Louisiana Board of Regents for the Louisiana Materials Design Alliance (LAMDA). The high-performance computing resources provided by the Louisiana Optical Network Infrastructure (https://loni.org) were used for this work.

Appendix A. Supplementary data

Supplementary data to this article can be found online at https://doi.org/10.1016/j.polymer.2023.126114.

References

[1] W. Post, A. Susa, R. Blaauw, K. Molenveld, R.J.I. Knoop, A Review on the Potential and Limitations of Recyclable Thermosets for Structural Applications, vol. 60, 2019, pp. 359–388, https://doi.org/10.1080/15583724.2019.1673406.
[2] F. Xie, L. Huang, J. Leng, Y. Liu, Thermoset shape memory polymers and their composites, J. Intell. Mater. Syst. Struct. 27 (2016) 2433–2455, https://doi.org/10.1177/1045389X16634211.
[3] L. Lu, J. Pan, G. Li, G.L.-J. of M.C. A, U., Recyclable high-performance epoxy based on transesterification reaction, J Mater Chem A Mater 5 (2017) 21505–21513, https://doi.org/10.1039/c7ta06397k, 2017.
[4] X. Feng, J. Fan, A. Li, G. Li, Multireusable thermoset with anomalous flame-triggered shape memory effect, ACS Appl. Mater. Interfaces 11 (2019) 16075–16086, https://doi.org/10.1021/acsami.9b03092.
[5] A. Li, A. Challapalli, G. Li, 4D printing of recyclable lightweight architectures using high recovery stress shape memory polymer, Sci. Rep. 9 (2019) 1–13, https://doi.org/10.1038/s41598-019-44110-9.
[6] X. Feng, G. Li, Versatile phosphate diester-based flame retardant vitrimers via catalyst-free mixed transesterification, ACS Appl. Mater. Interfaces 12 (2020) 57486–57496, https://doi.org/10.1021/ACSAMI.0C18852/SUPPL_FILE/AM0C18852_SI_004.MP4.
[7] G. Li, D. Nettles, Thermomechanical characterization of a shape memory polymer based self-repairing syntactic foam, Polymer 51 (2010) 755–762, https://doi.org/10.1016/J.POLYMER.2009.12.002.
[8] X. Lan, Y. Liu, H. Lv, X. Wang, J. Leng, S. Du, Fiber reinforced shape-memory polymer composite and its application in a deployable hinge, Smart Mater. Struct. 18 (2009), 024002, https://doi.org/10.1088/0964-1726/18/2/024002.
[9] G. Li, T. Xu, Thermomechanical characterization of shape memory polymer–based self-healing syntactic foam sealant for expansion joints, J. Transport. Eng. 137 (2011) 805–814, https://doi.org/10.1061/(ASCE)TE.1943-5436.0000279.
[10] M. Magzoub, S. Salehi, G. Li, J. Fan, C. Teodoriu, Loss circulation prevention in geothermal drilling by shape memory polymer, Geothermics 89 (2021), 101943, https://doi.org/10.1016/J.GEOTHERMICS.2020.101943.
[11] A. Mansour, A. Dahi Taleghani, S. Salehi, G. Li, C. Ezeakacha, Smart lost circulation materials for productive zones, J. Pet. Explor. Prod. Technol. 9 (2019) 281–296, https://doi.org/10.1007/s13202-018-0458-z.
[12] M. Behl, A. Lendlein, Shape-memory polymers, Mater. Today 10 (2007) 20–28, https://doi.org/10.1016/S1369-7021(07)70047-0.
[13] H. Meng, G. Li, A review of stimuli-responsive shape memory polymer composites, Polymer 54 (2013) 2199–2221, https://doi.org/10.1016/J.POLYMER.2013.02.023.
[14] H. Lu, W.M. Huang, On the origin of the Vogel–Fulcher–Tammann law in the thermo-responsive shape memory effect of amorphous polymers, Smart Mater. Struct. 22 (2013), 105021, https://doi.org/10.1088/0964-1726/22/10/105021.
[15] S. Tibbits, 4D printing: multi-material shape change, Architect. Des 84 (2014) 116–121, https://doi.org/10.1002/AD.1710.
[16] X. Kuang, D.J. Roach, J. Wu, C.M. Hamel, Z. Ding, T. Wang, M.L. Dunn, H.J. Qi, Advances in 4D printing: materials and applications, Adv. Funct. Mater. 29 (2019), 1805290, https://doi.org/10.1002/ADFM.201805290.
[17] H. Wu, P. Chen, C. Yan, C. Cai, Y. Shi, Four-dimensional printing of a novel acrylate-based shape memory polymer using digital light processing, Mater. Des. 171 (2019), 107704, https://doi.org/10.1016/J.MATDES.2019.107704.
[18] X. Wan, L. Luo, Y. Liu, J. Leng, Direct ink writing based 4D printing of materials and their applications, Adv. Sci. 7 (2020), 2001000, https://doi.org/10.1002/ADVS.202001000.
[19] B. Steyrer, B. Busetti, G. Harakály, R. Liska, J. Stampfl, Hot Lithography vs. room temperature DLP 3D-printing of a dimethacrylate, Addit. Manuf. 21 (2018) 209–214, https://doi.org/10.1016/J.ADDMA.2018.03.013.
[20] J.H.R. Clarke, D. Brown, Molecular dynamics modelling of polymer materials, Mol. Simulat. 3 (1989) 27–47, https://doi.org/10.1080/08927028908034618.
[21] J. Diani, K. Gall, Molecular dynamics simulations of the shape-memory behaviour of polyisoprene, Smart Mater. Struct. 16 (2007) 1575, https://doi.org/10.1088/0964-1726/16/5/011.
[22] B.C. Abberton, W.K. Liu, S. Keten, Coarse-grained simulation of molecular mechanisms of recovery in thermally activated shape-memory polymers, J. Mech. Phys. Solid. 61 (2013) 2625–2637, https://doi.org/10.1016/j.jmps.2013.08.003.
[23] J. Moon, J. Choi, M. Cho, Programmed shape-dependence of shape memory effect of oriented polystyrene: a molecular dynamics study, Polymer 102 (2016) 1–9, https://doi.org/10.1016/j.polymer.2016.08.096.
[24] J.D.J. Davidson, N.C. Goulbourne, N.G. S.M, N.C. Goulbourne, Microscopic mechanisms of the shape memory effect in crosslinked polymers, Smart Mater. Struct. 24 (2015), https://doi.org/10.1088/0964-1726/24/5/055014.
[25] M. Amini, K. Hasheminejad, A. Montazeri, Experimentally guided MD simulation to enhance the shape memory behavior of polymer-based nanocomposites: towards

elaborating the underlying mechanism, Structures, undefined 2015, Composer Part A Appl Sci Manuf 138 (2020), 106055, https://doi.org/10.1016/j.compositesa.2020.106055.
[26] A. Torres-Knoop, I. Kryven, V. Schamboeck, P.D. Iedema, Modeling the free-radical polymerization of hexanediol diacrylate (HDDA): a molecular dynamics and graph theory approach, Soft Matter 14 (2018) 3404–3414, https://doi.org/10.1039/c8sm00451j.
[27] A. Li, J. Fan, G. Li, Recyclable thermoset shape memory polymers with high stress and energy output: via facile UV-curing, J Mater Chem A Mater 6 (2018) 11479–11487, https://doi.org/10.1039/c8ta02644k.
[28] L.S. Dodda, I.C. De Vaca, J. Tirado-Rives, W.L. Jorgensen, LigParGen web server: an automatic OPLS-AA parameter generator for organic ligands, Nucleic Acids Res. 45 (2017) W331, https://doi.org/10.1093/nar/gkx312. –W336.
[29] D. Weininger, SMILES, a chemical language and information system: 1: introduction to methodology and encoding rules, J. Chem. Inf. Comput. Sci. 28 (1988) 31–36, https://doi.org/10.1021/ci00057a005.
[30] W.L. Jorgensen, J. Tirado-Rives, The OPLS [optimized potentials for liquid simulations] potential functions for proteins, energy minimizations for crystals of cyclic peptides and crambin, J. Am. Chem. Soc. 110 (1988) 1657–1666, https://doi.org/10.1021/ja00214a001.
[31] W.L. Jorgensen, J.D. Madura, C.J. Swenson, Optimized intermolecular potential functions for liquid hydrocarbons, J. Am. Chem. Soc. 106 (1984) 6638–6646, https://doi.org/10.1021/ja00334a030.
[32] W.L. Jorgensen, D.S. Maxwell, J. Tirado-Rives, N. Haven, Development and testing of the OPLS all-atom force field on conformational energetics and properties of organic liquids, J. Am. Chem. Soc. 118 (1996) 11225–11236, https://doi.org/10.1021/ja9621760.
[33] U. Essmann, L. Perera, M.L. Berkowitz, T. Darden, H. Lee, L.G. Pedersen, A smooth particle mesh Ewald method, J. Chem. Phys. 103 (1995) 8577–8593.
[34] C.D. Wick, A.J. Peters, G. Li, Quantifying the contributions of energy storage in a thermoset shape memory polymer with high stress recovery: a molecular dynamics study, Polymer 213 (2021), https://doi.org/10.1016/j.polymer.2020.123319 submitted for publication.
[35] A. Shafe, C.D. Wick, A.J. Peters, X. Liu, G. Li, Effect of atomistic fingerprints on thermomechanical properties of epoxy-diamine thermoset shape memory polymers, Polymer 242 (2022), 124577, https://doi.org/10.1016/j.polymer.2022.124577.
[36] S. Plimpton, Fast parallel algorithms for short-range molecular dynamics, J. Comput. Phys. 117 (1995) 1–19, https://doi.org/10.1006/jcph.1995.1039.
[37] R. Auhl, R. Everaers, G.S. Grest, K. Kremer, S.J. Plimpton, Equilibration of long chain polymer melts in computer simulations, J. Chem. Phys. 119 (2003) 12718–12728.
[38] LAMMPS Molecular Dynamics Simulator, http://lammps.sandia.gov, (n.d.).
[39] G.J. Martyna, M.L. Klein, M. Tuckerman, Nose-hoover chains - the canonical ensemble via continuous dynamics, J. Chem. Phys. 97 (1992) 2635–2643.
[40] S. Nosé, A unified formulation of the constant temperature molecular dynamics methods, J. Chem. Phys. 81 (1984) 511–519, https://doi.org/10.1063/1.447334.
[41] H.C. Andersen, Rattle: a "velocity" version of the shake algorithm for molecular dynamics calculations, J. Comput. Phys. 52 (1983) 24–34.
[42] M. Anthamatten, K. Cavicchi, G. Li, A. Wang, Cold, warm, and hot programming of shape memory polymers, J. Polym. Sci. B Polym. Phys. 54 (2016) 1319–1339, https://doi.org/10.1002/POLB.24041.
[43] J. Han, R.H. Gee, R.H. Boyd, Glass transition temperatures of polymers from molecular dynamics simulations, Macromolecules 27 (1994) 7781–7784.
[44] C. Li, A. Strachan, Molecular scale simulations on thermoset polymers: a review, J. Polym. Sci. B Polym. Phys. 53 (2015) 103–122, https://doi.org/10.1002/polb.23489.
[45] J. Fan, G. Li, High enthalpy storage thermoset network with giant stress and energy output in rubbery state, Nat. Commun. 9 (2018) 642, https://doi.org/10.1038/s41467-018-03094-2.
[46] C.D. Wick, A.J. Peters, G. Li, Quantifying the contributions of energy storage in a thermoset shape memory polymer with high stress recovery: a molecular dynamics study, Polymer 213 (2021), 123319, https://doi.org/10.1016/j.polymer.2020.123319.
[47] C. Yan, X. Feng, C. Wick, A. Peters, G. Li, Machine learning assisted discovery of new thermoset shape memory polymers based on a small training dataset, Polymer 214 (2021), https://doi.org/10.1016/j.polymer.2020.123351.
[48] P. Nourian, C.D. Wick, G. Li, A.J. Peters, Correlation between cyclic topology and shape memory properties of an amine-based thermoset shape memory polymer: a coarse-grained molecular dynamics study, Smart Mater. Struct. 31 (2022), 105014, https://doi.org/10.1088/1361-665X/ac8bb5.